Research Article

Elena Ferretti*

Satisfying Boundary Conditions in Homogeneous, Linear-Elastic and Isotropic Half-Spaces Subjected to Loads Perpendicular to the Surface: Distributed Loads on Adjacent Contact Areas

https://doi.org/10.1515/cls-2019-0002
Received Jun 29, 2018; accepted Jul 23, 2018

Abstract: This work originates from an experimental program on strain distribution near the loaded surface of an airfield concrete pavement, which provided us with results that contrast with the rheological predictions of Boussinesq for a homogeneous, linear-elastic and isotropic half-space. We already reviewed and extended the original work carried out by Boussinesq in previous papers, to provide a closed form second order solution that enabled us to establish a good match between analytical and experimental findings for point-loads. In this paper, we have explained why Boussinesq's closed form solution for a homogeneous linear-elastic and isotropic half-space subjected to a point-load is not exact, as believed until now, but approximated. Then, we have shown that our second order solution is the actual solution of Boussinesq's problem. We have also presented the numerical analysis of second order for rectangular and elliptical contact areas, both loaded by uniform and parabolic laws of external pressure. Moreover, we have evaluated the interaction effect provided on the surface of a concrete half-space by the twin wheels of an aircraft landing gear. Extension of the solution to layered systems is also possible, for improving the knowledge of stress propagation into airfield pavements and promoting more effective design standards.

Keywords: Boussinesq's problem, Non-uniform Load, Interaction Effect, Airfield Concrete Pavement, Twin Wheels

1 Introduction

The present study follows an experimental program undertaken at the Guglielmo Marconi airport of Bologna (Italy) for acquiring pavement strains at aircraft taxiing, by means of some strain gauges embedded into the concrete slab of the taxiway (Figure 1, [1]).

Figure 1: Rehabilitation interview of the taxiway at the Guglielmo Marconi airport of Bologna (Italy): area of the rehabilitation interview boxed in red and experimental segment filled in red (from [2].)

After stress identification, we found that the vertical stresses transmitted to the pavement depend on the elastic properties of concrete [1]. Moreover, the profile of the acquired strains for static load (Figure 26 of [2]) is very similar to the form of the wave propagating along the rail foregoing the wheel for static load (Figure 3 of [3]). This means that around the tire/pavement contact areas there are some vertical tensile stresses (Figure 2, [2]) that are not caused by friction forces, since they appear even when the speed is very low, that is, in quasi-static conditions.

Both the dependence of the vertical stresses on concrete elastic properties and the presence of tensile stresses around the contact areas are not accounted by Boussinesq's closed form elastic solution for a homogeneous, linear-elastic and isotropic half-space subjected to a point-

*Corresponding Author: Elena Ferretti: DICAM – Department of Civil, Chemical, Environmental, and Materials Engineering, Alma Mater Studiorum, Università di Bologna, Viale del Risorgimento 2, 40136 (BO), Italy; Email: elena.ferretti2@unibo.it; Tel.: +39-051-209-35-15; Fax.: +39-051-209-34-95

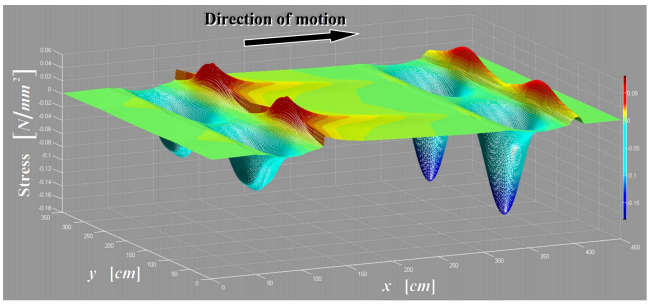

Figure 2: Vertical stresses induced near the surface by the front and back wheels (from [2]).

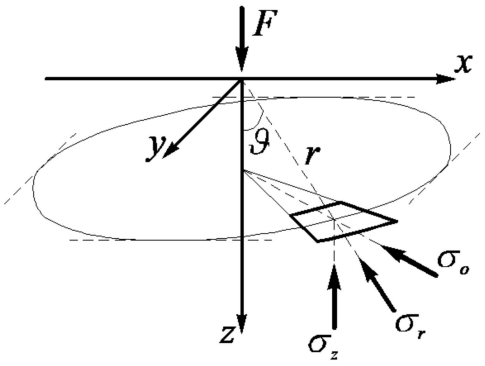

Figure 3: Parameter definition for Eq. (1).

load perpendicular to the surface [4, 5]:

$$\sigma_z = \frac{3}{2}\frac{F}{\pi r^2}\cos^3\vartheta \tag{1}$$

where σ_z is the vertical stress at the distance r between the application and the evaluation points, ϑ is the angle between the point load vector and the radial arm connecting the application to the evaluation point, and F is the point-load applied at the surface (Figure 3).

In fact, from Eq. (1) we can see that σ_z is independent of the elastic properties of the transmitting medium and has the same sign as F independently of the distance from the application point.

The inconsistencies between Boussinesq's solution and our experimental findings led us to a review of the original work carried out by Boussinesq [6], in the search for a higher order closed elastic solution for the homogeneous, linear-elastic and isotropic half-space subjected to a point-load perpendicular to the surface. It is worth noting that, even in the past, a number of numerical and empirical models proposed modifications to Boussinesq's solution based on several inconsistencies between Boussinesq's solution and the experimental evidence [7–18]: the most relevant inconsistency they took into account is that, for most cases, Boussinesq's solution results in stresses and deflections that are greater than the measured values.

Indeed, Boussinesq was himself aware that Eq. (1) may not have been valid for non-solid materials and had developed a theory for stresses in a granular medium, assuming the shear modulus to be proportional to the hydrostatic stress [5]. Well, each of those modified old models is able to capture some experimental behavior, but none of them predicts the tensile stresses that we identified near the surface [1, 2]. On the contrary, our new closed form elastic solution [6] succeeds in explaining why a compression point-load induces both compression and tensile stresses into the homogeneous, linear-elastic and isotropic half-space. It also provides stresses and deflections lower than those of Boussinesq.

2 A comparison between Boussinesq's solution and the second order solution

We must recall that Boussinesq obtained Eq. (1) by using the theory of linear elasticity and the properties of potentials. In particular, he built the solution on the similarity between the system of equilibrium equations:

$$\begin{cases} (\lambda+\mu)\dfrac{\partial I_{1\varepsilon}}{\partial x} + \mu\nabla^2 u = 0 \\ (\lambda+\mu)\dfrac{\partial I_{1\varepsilon}}{\partial y} + \mu\nabla^2 v = 0 \\ (\lambda+\mu)\dfrac{\partial I_{1\varepsilon}}{\partial z} + \mu\nabla^2 w = 0 \end{cases} \tag{2}$$

where the body forces have been set to zero, since gravity has been neglected:

$$f_x = f_y = f_z = 0, \tag{3}$$

and the system of equations:

$$\begin{cases} \dfrac{\partial}{\partial x}\left(2\dfrac{\partial P}{\partial z}\right) - \nabla^2\dfrac{\partial (zP)}{\partial x} = 0 \\ \dfrac{\partial}{\partial y}\left(2\dfrac{\partial P}{\partial z}\right) - \nabla^2\dfrac{\partial (zP)}{\partial y} = 0 \\ \dfrac{\partial}{\partial z}\left(2\dfrac{\partial P}{\partial z}\right) - \nabla^2\dfrac{\partial (zP)}{\partial z} = 0 \end{cases} \tag{4}$$

that is satisfied by any potential function P for which the Laplacian is equal to zero:

$$\nabla^2 P = \frac{\partial^2 P}{\partial x^2} + \frac{\partial^2 P}{\partial y^2} + \frac{\partial^2 P}{\partial z^2} = 0. \tag{5}$$

The first expression for P chosen by Boussinesq is the logarithmic potential Ψ of the loaded surface for the prefixed point (x, y, z) of the semi-space under the surface, at

the distance r from the point $Q \equiv (x_1, y_1, 0)$ of the load surface:

$$P = \Psi = \int \log(z + r)\, dm \tag{6}$$

with:

$$\nabla^2 \Psi = 0 \tag{7}$$

$$r = \sqrt{(x - x_1)^2 + (y - y_1)^2 + z^2} \tag{8}$$

$$dm = dF = \rho(x_1, y_1)\, dx_1 dy_1 \tag{9}$$

where $\rho(x_1, y_1)$ is the mass density for unit surface at the point Q.

In order to comply with the actual displacement field at infinity ($r \to \infty$, Figure 4), which declines at infinity as rapidly as the function $1/r$, Boussinesq then used the first partial derivative $\partial\Psi/\partial z$ of Eq. (6), instead of the logarithmic potential Ψ, for the potential P in Eqs. (4):

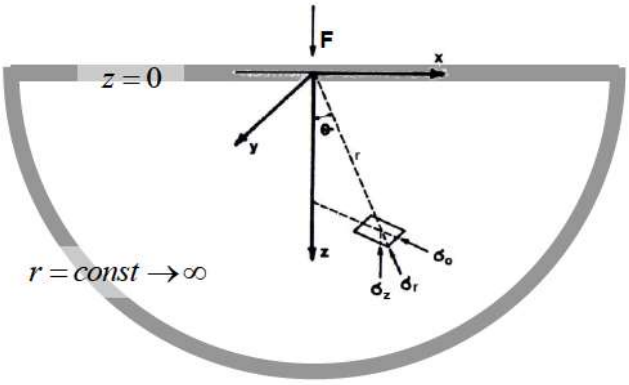

Figure 4: The boundary of the half-space.

$$P = \frac{\partial \Psi}{\partial z} = \int \frac{dm}{r}. \tag{10}$$

This substitution is allowable, since $\partial\Psi/\partial z$ still gives a Laplacian equal to zero:

$$\nabla^2 \frac{\partial \Psi}{\partial z} = 0. \tag{11}$$

Nevertheless, the choice made by Boussinesq in Eq. (10) is not sufficient for guaranteeing the well-posedness of the boundary value problem. In fact, worrying about meeting the boundary conditions for $r \to \infty$ is not enough, because the boundary of the half-space is made by both the loci $r \to \infty$ and $z = 0$ (Figure 4). Due to lacking of information on the stress and strain behavior at the surface, Boussinesq could not set a proper boundary condition for $z = 0$. Therefore, his solution satisfies the boundary conditions for $r \to \infty$ whereas does not comply with the boundary conditions for $z = 0$. Consequently, Boussinesq's solution for $z = 0$ is highly sensitive to changes in the given data, either for stresses or for displacements, particularly for $r \to 0$. According to the definition of well-posed problem [19], this makes Boussinesq's mathematical model ill-posed. For restoring well-posedness, we must comply with the boundary conditions along the entire contour of the half-space.

In conclusion, the solution of Boussinesq is not the exact solution of the elastic problem he studied and can be improved, particularly for $z = 0$.

We may rewrite Eq. (1) as:

$$\sigma_z = \frac{3}{2} \frac{F}{\pi z^2} \cos^5 \vartheta \tag{12}$$

or, in Cartesian coordinates:

$$\sigma_z = \frac{3}{2} \frac{F z^3}{\pi r^5}. \tag{13}$$

Further forms of Eq. (1) in Cartesian coordinates are:

$$\sigma_z = \frac{3}{2} \frac{F z^3}{\pi \left(R^2 + z^2\right)^{\frac{5}{2}}} \tag{14}$$

where R is the horizontal distance from the application to the evaluation point, and:

$$\sigma_z = I_B \frac{F}{z^2}. \tag{15}$$

I_B, known as the influence factor, takes the form:

$$I_B = \frac{3}{2\pi} \left[1 + \left(\frac{R}{z}\right)^2\right]^{-\frac{5}{2}}. \tag{16}$$

It should be noted that, as previously pointed out for Eq. (1), in Eqs. (12), (13), (14), and (15) the vertical normal stress (σ_z) is independent of the elastic constants at a point: E, the longitudinal modulus of elasticity or Young's modulus, and υ, Poisson's ratio. That is, Boussinesq's vertical normal stress spreads in the medium independently of the kind of medium itself. Since our experimental program on stress identification in loaded concrete pavements provided evidence against this analytical result [1], we can now conclude that the independence of σ_z from the elastic constants is a false result, direct consequence of having satisfied the boundary conditions in part.

Boussinesq obtained the solution for a point-load perpendicular to the surface (infinitesimal load surface) by replacing the integrals with their integrands, that is, by causing the dimensions of the load surface in the x/y plane to vanish. This provides:

$$\sigma_z = -\frac{3}{2\pi} \frac{z^3}{r^5} dF \tag{17}$$

where the minus sign depends on the fact that the outgoing normal versor, n, on each horizontal plane at the depth z is opposite to the z axis, whose direction is that of gravity:

$$\boldsymbol{n} = \begin{bmatrix} n_x \\ n_y \\ n_z \end{bmatrix} = \begin{bmatrix} 0 \\ 0 \\ -1 \end{bmatrix}. \tag{18}$$

For a finite load F, Eq. (17) gives Eq. (13), where σ_z is a stress of compression. The vertical stress contours below a concentrated load form the ball-shaped surface shown in Figure 5.

In building our closed form solution, we followed the same analytical strategy as Boussinesq [6]. This second time, however, the point-load solution is obtained directly by defining the potentials for the infinitesimal superficial neighborhood of the point $(x_1, y_1, 0)$. Consequently, we set the logarithmic potential of the infinitesimal neighborhood of mass dm equal to:

$$\psi = \log(z + r)\, dm \tag{19}$$

which satisfies the condition:

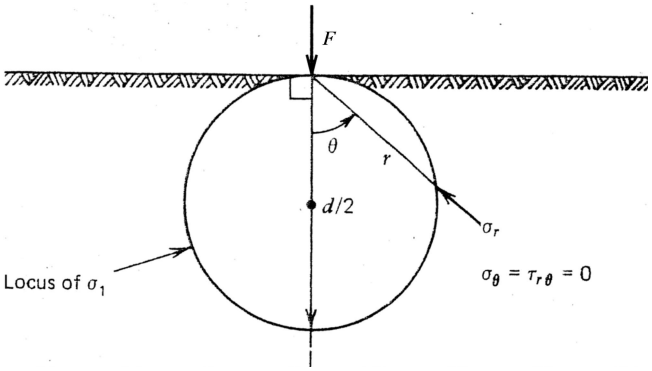

Figure 5: Stress distribution of Boussinesq (from [6]).

$$\nabla^2 \psi = 0. \tag{20}$$

If we take:

$$P = \frac{\partial \psi}{\partial z} = \frac{1}{r} dm \tag{21}$$

the solution obtained following Eqs. (4) and the assumption in Eq. (21) is:

$$\sigma_z = -3 \frac{z^3}{r^5} dF \tag{22}$$

which replaces Eq. (17).

Moreover, we further developed Boussinesq's idea of replacing the potential with one of its partial derivatives, to provide a stress solution to the vertical point-load problem that also depends on the elastic constants [6]. In fact, following the spirit of the superposition principle and noting that the partial derivatives of any arbitrary order of the function ψ have a zero Laplacian (*i.e.* they satisfy the condition $\nabla^2 = 0$), it is possible to refine the approximated elastic solution provided by Boussinesq by adding to it a further solution of Eqs. (4), obtained by replacing ψ with one of its derivatives. By choosing the derivatives of the second order [6], we found the second order solution:

$$\sigma_z = \frac{-1}{r^3} \left[3\frac{z^3}{r^2} + 2C\mu \left(15\frac{z^4}{r^4} - 3\frac{2\lambda + \mu}{\lambda + \mu}\frac{z^2}{r^2} - \frac{\lambda + 2\mu}{\lambda + \mu} \right) \right] dm \tag{23}$$

where:

$$r \neq 0 \tag{24}$$

$$\lambda = E\frac{\upsilon}{(1 + \upsilon)(1 - 2\upsilon)} \tag{25}$$

$$\mu = G = \frac{E}{2(1 + \upsilon)}. \tag{26}$$

Thus, as expected, it is possible to build a closed form elastic solution that puts σ_z in relationship with the elastic constants E and υ. In particular, the terms that refine Eq. (22) – that is, the terms in round brackets of Eq. (23), multiplied by $-2C\mu/r^3$ – significantly modify the normal stress when approaching the surface, whereas they are negligible at great depths. In fact, for $z \to 0$:

$$-p_z = \lim_{z \to 0} \sigma_z = 2C\mu \frac{\lambda + 2\mu}{\lambda + \mu} \frac{1}{r^3} dm \tag{27}$$

which depends on the elastic constants, whereas, for $z \to \infty$, Eq. (23) gives the first order solution:

$$\lim_{z \to \infty} \sigma_z = -3\frac{z^3}{r^5} dm \tag{28}$$

which, for the position in Eq. (9), is equal to Eq. (22). As can be easily verified, for $z \to \infty$ the solution proposed in [6] is equal to the solution of Boussinesq even for the displacement field.

Note that, in the assumption $C > 0$, the normal stress given by Eq. (27) for $z \to 0$ is opposite in sign to the normal stress given by Eq. (28) for $z \to \infty$. This allows the vertical stresses to change sign in function of the distance from the application point.

The contour lines of Eq. (23) are given in Figure 6 for a prefixed υ and variable values of E, and in Figure 7 for a prefixed E and variable values of υ [20]. As we can see in both Figure 6 and Figure 7, two families of stress contours, one of tensile stresses and the other of compression stresses, now distinguish the solution. The contour line that separates the two families (the locus $\sigma_z = 0$)

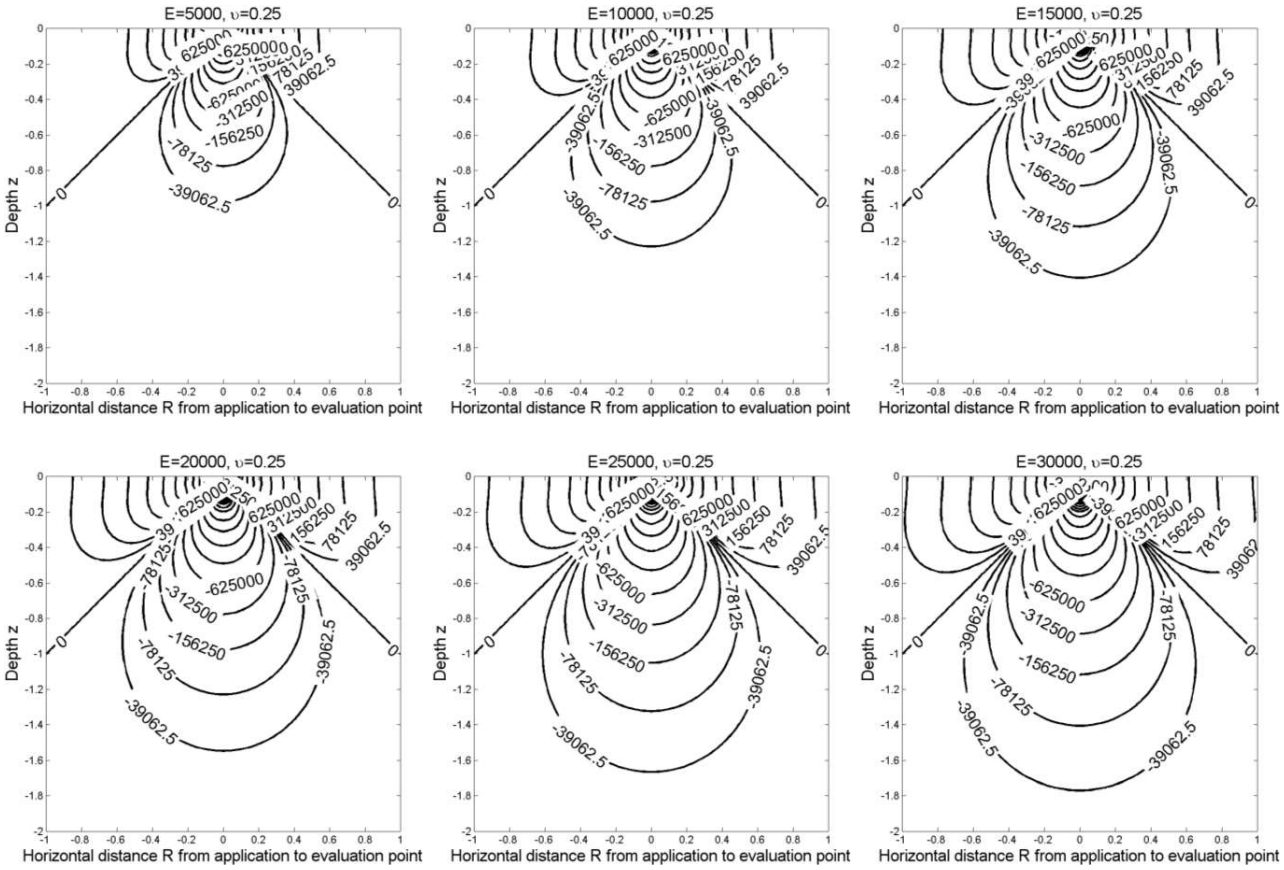

Figure 6: Parametric analysis on E for the vertical stress contours (all distances in mm) (from [6]).

does not depend on Young's modulus (Figure 6), whereas it slightly depends on Poisson's ratio (Figure 7). Lastly, the family of compression stresses is no longer ball-shaped, like that in Figure 5. The new drop-shaped stress contours for compression stresses in some way resemble the stress contours of several empirical modified models and, specifically, those of Fröhlich's modified model [11]:

$$\sigma_z = \frac{n}{2}\frac{Fz^n}{\pi r^{n+2}}. \tag{29}$$

In point of fact, when the concentration factor of Fröhlich, n, is equal to 3, Eq. (29) provides the Boussinesq equation, whereas, for $n > 3$, Eq. (29) increases the depth at which the stresses propagate so that the stress contours protrude more deeply into the elastic medium, changing the ball-shaped surface of Figure 5 into an ellipsoidal-shaped surface (Figure 8). Values of n greater than 3 are used specifically to predict soil compaction resulting from heavy tractor tires, since it was found that agricultural soils distribute stresses differently from the ball-shaped surfaces shown in Figure 5 [21]: soil stresses are greater under the load axis and smaller further away.

In [6], we showed that Eq. (27) matches the stresses identified for $z \to 0$ in the experimental campaign [1]. This means that Eq. (23) complies with the boundary conditions for $z \to 0$. Moreover, since Eqs. (9) and (28) demonstrate that, for $r \to \infty$, Eq. (23) provides the same stresses as Eq. (22), Eq. (23) inherits the complying with the boundary conditions for $r \to \infty$ from Boussinesq's solution. Consequently, the new solution for σ_z satisfies the boundary conditions along the entire contour of the domain. Thus, uniqueness of the solution for well-posed elastic problems [19] allows us to state that the second order solution given by Eq. (23) not only improves Boussinesq's solution: it is the actual closed form solution of Boussinesq's problem. This makes it unnecessary to employ empirical modified models for capturing the experimental behavior.

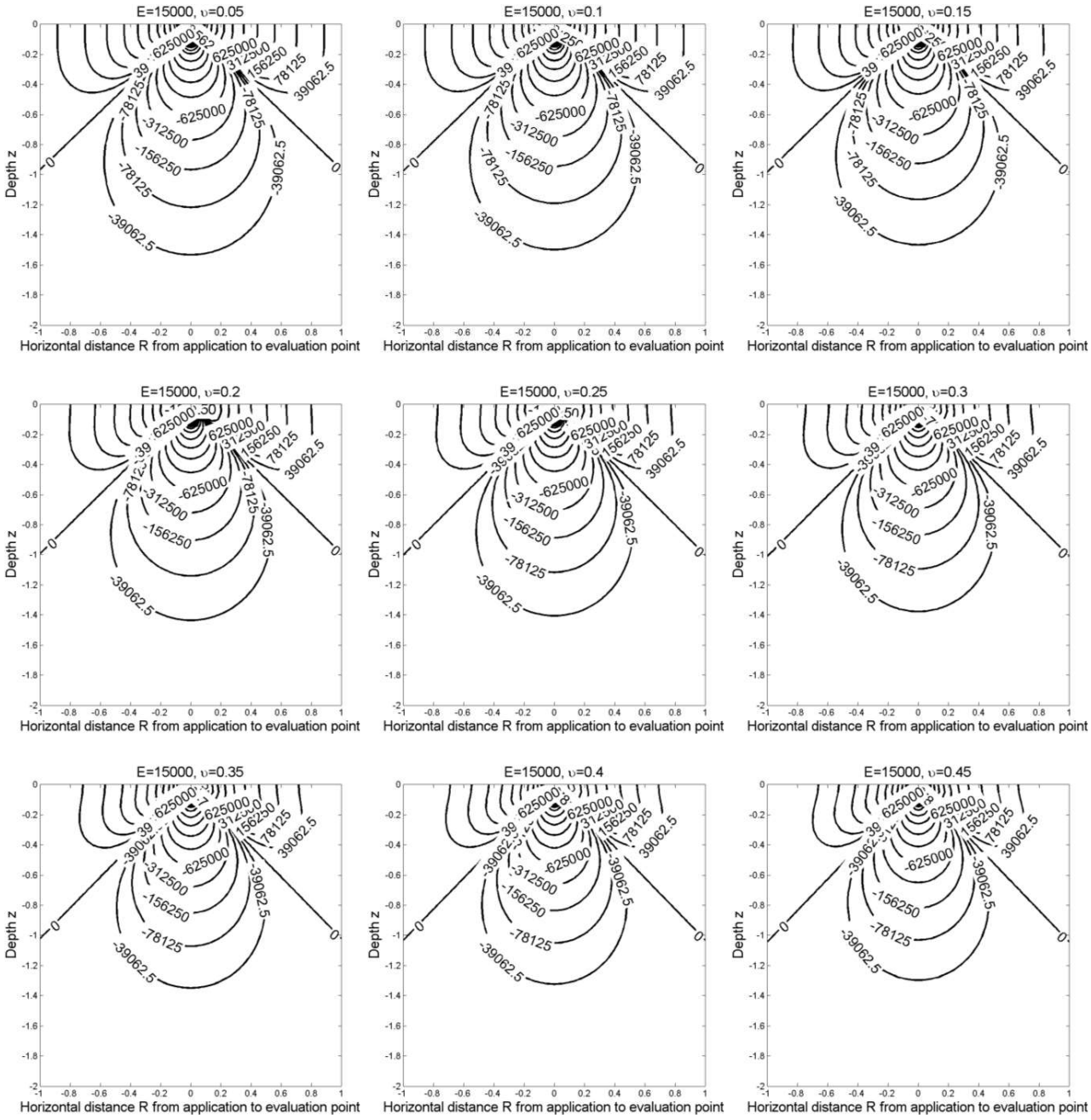

Figure 7: Parametric analysis on υ for the vertical stress contours (all distances in mm) (from [6]).

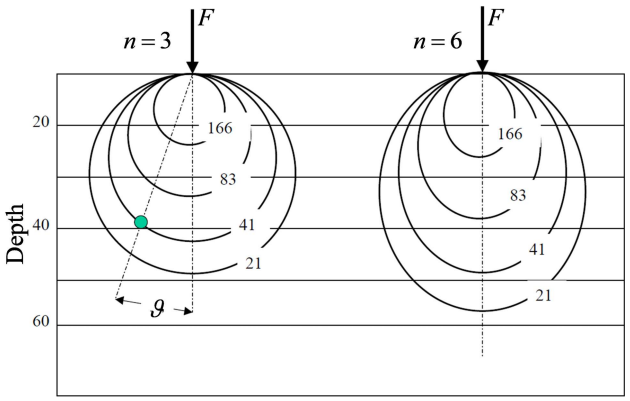

Figure 8: Fröhlich's curves of equal vertical normal stress in the elastic medium (from [6]).

3 Numerical results of second order for contact areas greater than zero

Variation of stress with depth for the case of load distributed over a contact area greater than zero follows the same general pattern as for the point-load case.

Some of the most important fields of application for Boussinesq's problem are the design of airfield pavements [1, 2, 22] and soil compaction modeling in agricultural soils [23]. In both cases – and, for the first case, particularly when the airfield pavement is a flexible pavement (Figure 9) – tire pressure and the extent of the tire-ground contact area affect the intensity of stress at a given point. Moreover, the major difference in stress intensities caused by variation in tire pressure occurs near the surface. Consequently, the surface course and base course of a flexible pavement (Figure 9) are the most seriously affected by high tire pressures. Finally, even the shape of the tire-ground contact area and the load profile depend upon the tire pressure. This makes modeling tire-ground interaction particularly complex.

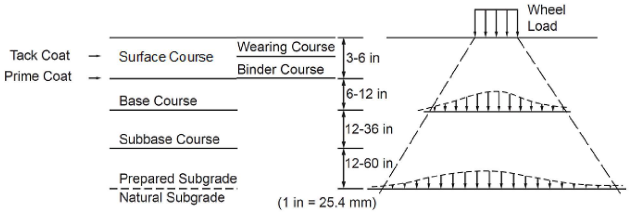

Figure 9: Cross section and stress distribution in a flexible pavement: since the loaded area increases with depth, the further down the layer is in the pavement structure, the fewer loads it must carry (from [1]).

Since the shape of both the contact area and the load profile exercise an influence over the vertical stress distribution with depth, in the following part of the paper, we have examined and compared two contact area shapes, each loaded by two different stress profiles.

We will investigate only the stresses induced by static loads [24, 25], which become superimposed on the stresses induced by moving loads [26, 27], dynamic loads [28, 29], and sliding loads [30–34] to provide the stress distribution of Figure 2. We will not take into account even nanoindentation [35, 36]. The reason why we have studied only static loads is that the critical areas of an airfield pavement are those where the aircraft speed is low or the aircraft is at rest (aprons, hard standings, taxiways, runway ends, turnoff ramp, and hangar floors).

Detrimental effects of fuel spillage, severe jet blast and long lasting loads occur very often in critical areas. In those areas, one should possibly avoid the use of flexible pavements. In fact, fuel spillage leaches out the asphalt cement in asphaltic pavements and jet blast damages bituminous pavements when the intense heat impinges in one area long enough to burn or soften the bitumen, so that the blast erodes the pavement. Moreover, the higher stiffness of rigid pavements (Figure 10) is recommended in critical areas, in order to avoid wheel ruts due to repeated tracking of aircraft and equipment. For all these reasons, we chose to replace the original flexible pavement of the taxiway at the Guglielmo Marconi airport of Bologna with a rigid pavement (Figure 1), made of concrete slabs resting on a subbase [37, 38]. We carried out the computational analysis accordingly, by considering vertical loads applied to the surface of concrete half-spaces.

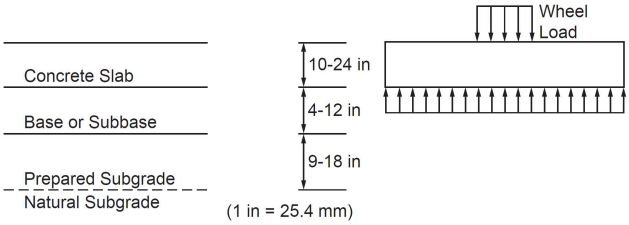

Figure 10: Cross section and stress distribution in a rigid pavement (from [1]).

3.1 Rectangular contact area

The simplest model we can assume for tire-ground interaction is that of uniform load over a rectangular contact area (Figure 11), where the longer side of the rectangular con-

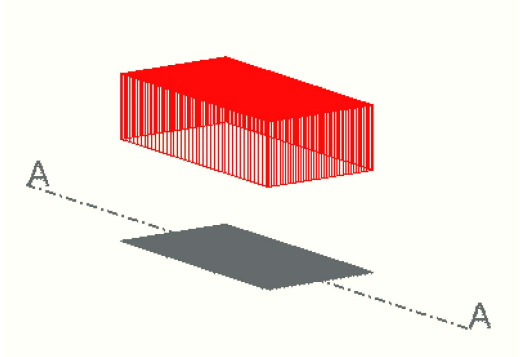

Figure 11: Uniform load distribution over a rectangular tire-ground contact area (the A-A vertical section is taken along the cross-section of the wheel).

tact area is in the direction of the wheel thickness, and the shorter side is in the direction of the wheel diameter (motion direction). The σ_z contours on the A-A vertical cross-section (orthogonal to the direction of motion) are shown in Figure 12 for both the solution of Boussinesq and the second order solution given by Eq. (23).

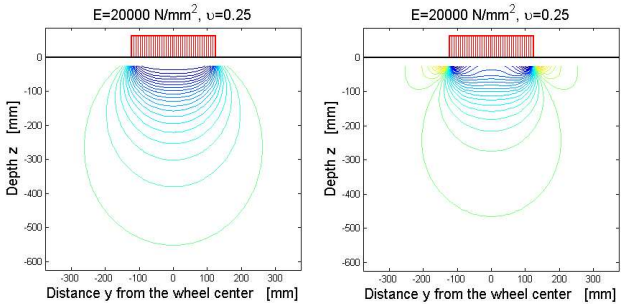

Figure 12: σ_z contours on the A-A vertical cross-section of Figure 11: Boussinesq's solution on the left and the second order solution on the right.

As for the point-load case, even in this case the second order solution is composed of two families of stress contours, one for the tensile stresses and one for the compression stresses. Moreover, the shape of the compression stress contours of second order changes with depth: at great depths, they are similar to the compression stress contours of Boussinesq's solution, whereas near the surface, they indicate that the negative stresses concentrate at the ends of the contact area. In Boussinesq's solution, on the contrary, the superficial stress contours are very flat, indicating an almost uniform distribution of stresses under the contact area. The reason why the solution of Boussinesq and the second order solution behave differently near the surface, but not at depth, is ultimately a consequence of Eqs. (27) and (28).

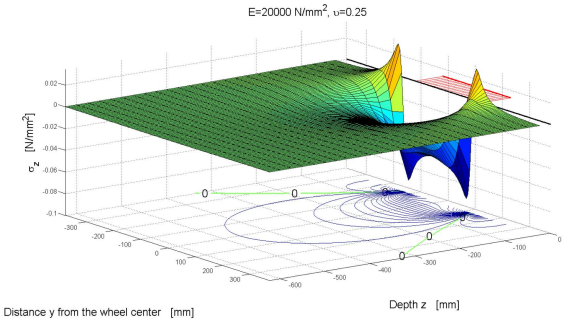

Figure 13: 3-D surface and stress contours of σ_z on the A-A vertical cross-section of Figure 11, according to the second order solution.

In Figure 12, we can see that the positive stresses also concentrate near, but in this case just outside, the ends of the contact area. The contour of the contact area is, therefore, a very critical zone where stresses rapidly pass from their maximum positive value to their maximum negative value. A more detailed view of this behavior is provided in Figure 13, where the second order solution for σ_z is depicted along the third (vertical) axis. Figure 13 also gives us an idea of how rapidly the positive stresses decline with depth.

In Figure 14, we have plotted the stress profiles near the surface, whereas, in Figure 15, they are plotted for $z = -75$ mm, the depth at which the concentration effect of the negative stresses along the A-A cross-section is almost completely extinguished. A comparison between the right-hand sides of Figures 14 and 15 shows that the ratio between the maximum negative stress (in absolute value) and the maximum positive stress increases with depth. Moreover, as we can see in both Figures 14 and 15, the compressive stresses predicted by the second order solution are sensitively lower (in absolute value) than those predicted by Boussinesq for the same external load. This

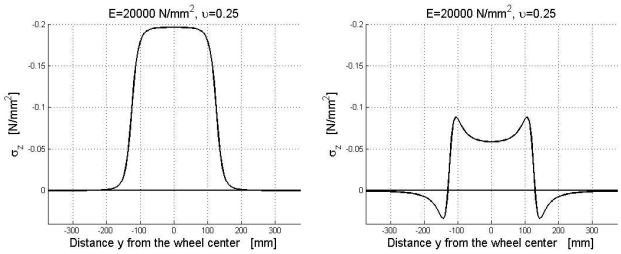

Figure 14: Superficial profiles of σ_z on the A-A vertical cross-section of Figure 11: Boussinesq's solution on the left and the second order solution on the right.

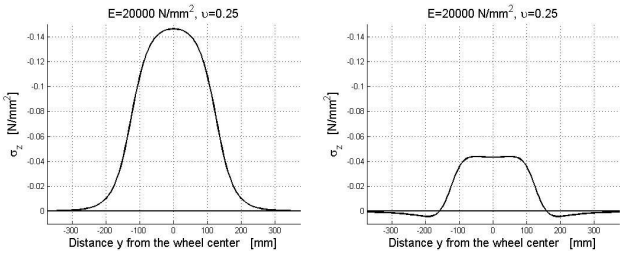

Figure 15: Profiles of σ_z on the A-A vertical cross-section of Figure 11 for $z = -75$ mm: Boussinesq's solution on the left and the second order solution on the right.

is a good result since, as we have previously pointed out, Boussinesq overestimates both stresses and deflections. Note also that the graphs to the right of Figures 14 and 15 were obtained making the assumption of convenience that the constant C in Eq. (23) is equal to 1. Obviously, it is always possible to calibrate C in order to match the experimental data better.

The complete representation of σ_z on the horizontal plane near the surface is given in Figure 16, where x is the distance from the wheel centre computed along the motion direction and y is the distance from the wheel centre computed along the cross-section. In Figure 16, we can gain a better appreciation of the effect of stress concentration under the contour of the contact area for both the negative and the positive stresses of the second order solution. In particular, the negative stresses reach their highest values under the corners of the contact area, whereas the positive stresses reach their highest values under the middle points of the sides. Moreover, the maximum positive stress along the longer sides is higher than the maximum positive stress along the shorter sides.

Note that the 3-D surfaces in Figure 16 have two planes of symmetry (the planes $x = 0$ and $y = 0$) because we plotted the 3-D surfaces for static loads. It must be recalled that the existence of two positive peaks of equal intensity, one before and one after the wheel, is compatible with the experimental data for static loads described in [2], where we concluded that friction is not the main cause of the growing of tensile stresses inside the pavement, but interacts with them enhancing the positive stresses from one side of the wheel and decreasing the positive stresses from the other side. Actually, in the case of moving loads, the friction forces developed on the contacts areas would have a skew-symmetric effect on the shape of the 3-D surfaces of σ_z and the positive peaks on the right of Figure 16 would become more similar to those depicted in Figure 2, with the positive stresses on the back of the wheel weaker than the positive stresses on the front of the wheel. On the other

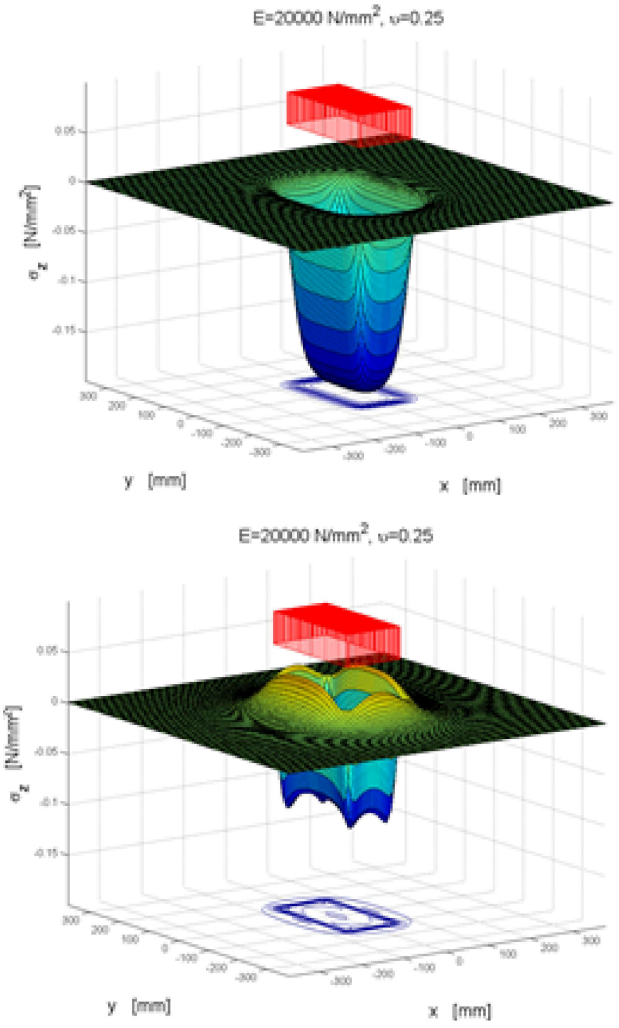

Figure 16: 3-D surfaces and stress contours of σ_z near the surface: Boussinesq's solution on the top and the second order solution on the bottom.

hand, however, when the aircraft speed is high the aircraft is already partially airborne. In effect, at the speed at which the aircraft passes over the pavement, on the wings of the aircraft there is enough lift to reduce the stresses applied to the pavement considerably. This is why the central portions of runways and the high-speed exit taxiways are noncritical areas. Even touchdown at the end of the runway may not be critical because the airplane is partially airborne. In conclusion, the static load equal to the maximum takeoff weight of the aircraft is actually the most interesting case as far as thickness design of airfield pavements is concerned.

Note also that the existence of tensile stresses when a load moves along a concrete pavement was assumed by several researchers, in the past [39–41], in order to explain some of the main mechanisms of pavement distress. More

precisely, the tensile stresses induced into pavements by moving loads were always assumed as horizontal stresses. Now we are able to explain those distresses analytically, at the same time making clear that the tensile stresses are vertical.

A more refined model of tire-ground interaction is that of a rectangular contact area with parabolic load profile along the cross-sections (Figure 17). In this second case also, the second order solution is composed of two families of stress contours of opposite sign, whereas the solution of Boussinesq only contemplates a single family of stress contours, the family of the negative stresses (Figure 18). Apart from this, there is a fundamental difference between the two load profiles: in the second case, the negative stresses σ_z of the second order solution do not concentrate everywhere under the contact area. They, in fact, do not concentrate along the direction of the parabolic load, that is, under the ends of the contact area on the cross-section in Figures 18 and 19 and under the ends of the contact area on all the vertical cross-sections that are parallel to A-A (Figure 20), including the vertical sections that pass through the longer sides of the contact area. Nevertheless, the negative stresses continue to concentrate along the direction where the load is uniformly distributed, that is, under the ends of the shorter sides and under the ends of the contact area for all the vertical sections that are orthogonal to A-A (Figure 20). We can conclude that the concen-

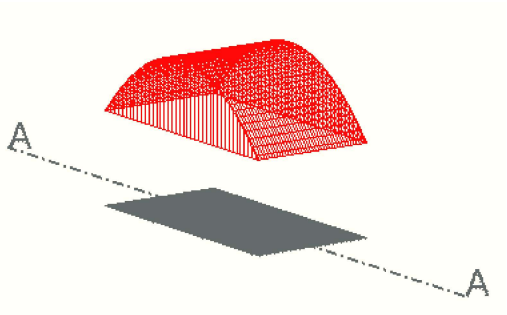

Figure 17: Parabolic load distribution along the cross-sections of a wheel with rectangular tire-ground contact area (the A-A vertical section is taken along the cross-section of the wheel).

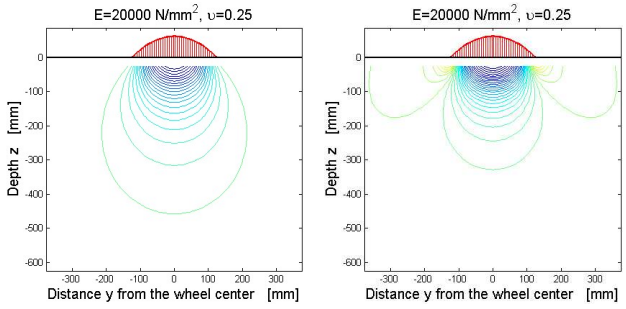

Figure 18: σ_z contours on the A-A vertical cross-section of Figure 17: Boussinesq's solution on the left and the second order solution on the right.

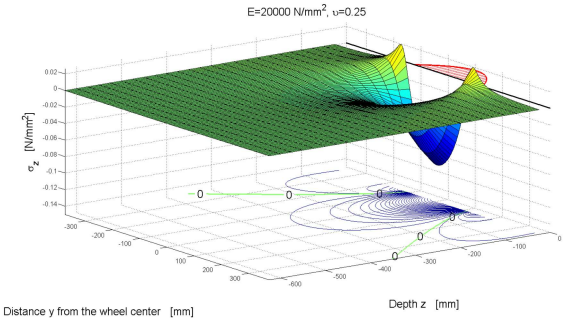

Figure 19: 3-D surface and stress contours of σ_z on the A-A vertical cross-section of Figure 17, according to the second order solution.

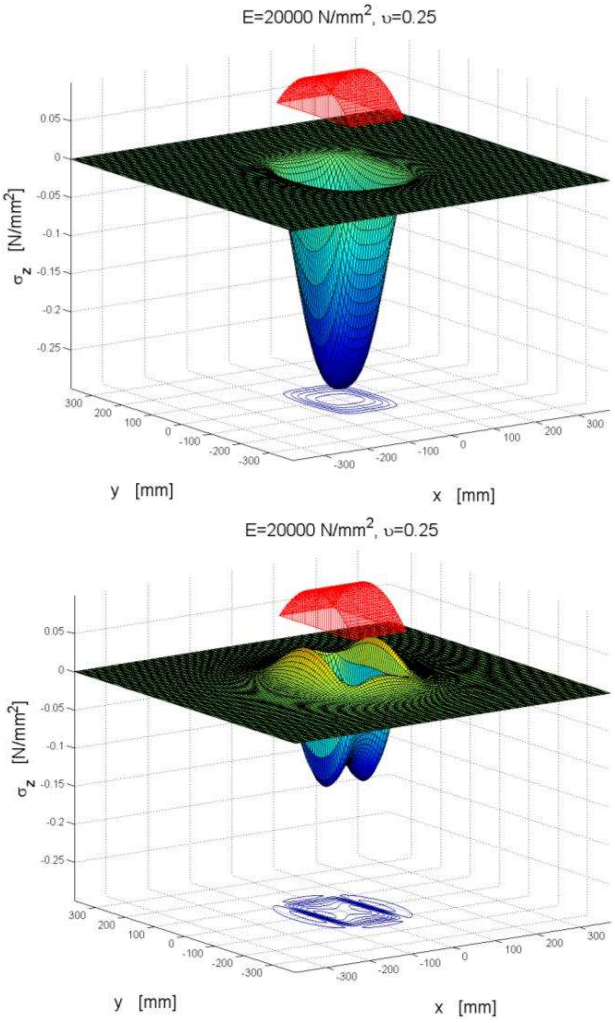

Figure 20: 3-D surfaces and stress contours of σ_z near the surface: Boussinesq's solution on the top and the second order solution on the bottom.

tration of the negative stresses arises whenever the load is uniformly distributed along one direction, under the ends of the load distribution.

The positive peaks of the second order solution, on the contrary, do not seem to depend upon the shape of the load profile, since the positive stresses concentrate near both the longer and the shorter sides of the contact area (Figure 20). The presence of a positive σ_z near the contour of the contact area does not, in fact, depend upon the load profile, but on the terms in round brackets of Eq. (23) (multiplied by $-2C\mu/r^3$), which refine the solution of Boussinesq. The contour of the contact area is therefore critical for tensile stresses, independently of the shape of the load profile. Moreover, as for the previous case, positive stresses reach their highest values under the middle points of the sides, with the maximum stress along the longer sides being higher than the maximum stress along the shorter sides. In Figure 20, we can also note that, as for the former model, the negative stresses predicted by the second order solution are sensitively lower (in absolute value) than the ones predicted by Boussinesq for the same external load.

3.2 Elliptical contact area

In this Section, we will consider the more realistic case of an interaction model with an elliptical contact area. Moreover, as for the rectangular contact area, we will consider both a uniform (Figure 21) and a parabolic load profile, which, in this case, is a paraboloid (Figure 24). The results of the stress analysis for an elliptical contact area are given in Figures 22, 23, 25, and 26.

The results substantially confirm the findings for a rectangular contact area. Specifically:

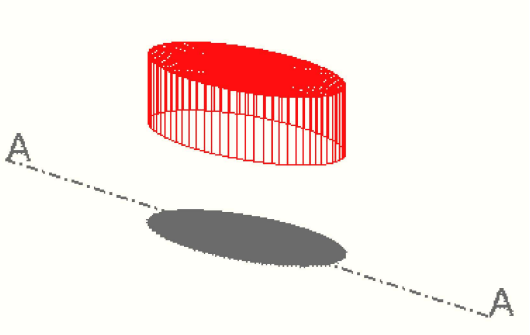

Figure 21: Uniform load distribution over an elliptical tire-ground contact area (the A-A vertical section is taken along the cross-section of the wheel).

- The second order solution predicts the presence of tensile stresses near the surface, which are absent in the solution provided by Boussinesq.

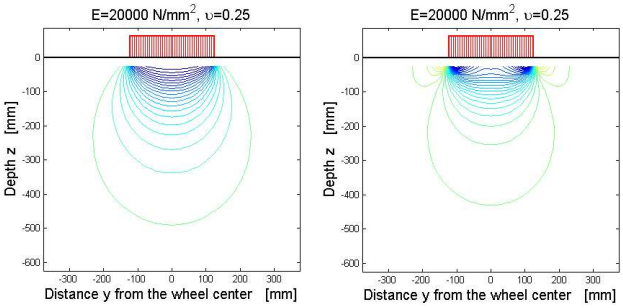

Figure 22: σ_z contours on the A-A vertical cross-section of Figure 21: Boussinesq's solution on the left and the second order solution on the right.

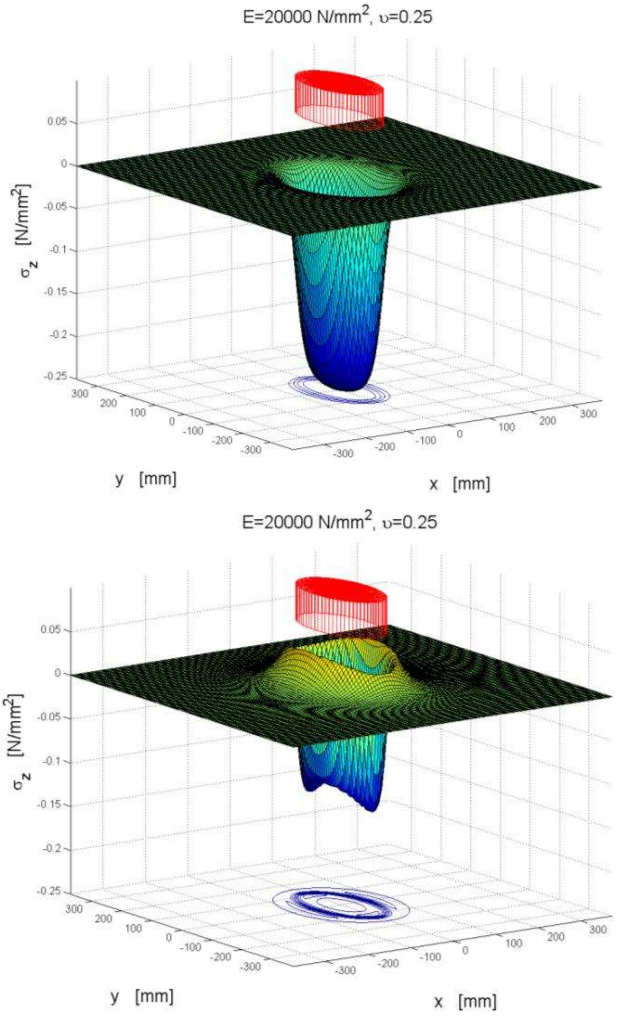

Figure 23: 3-D surfaces and stress contours of σ_z near the surface: Boussinesq's solution on the top and the second order solution on the bottom.

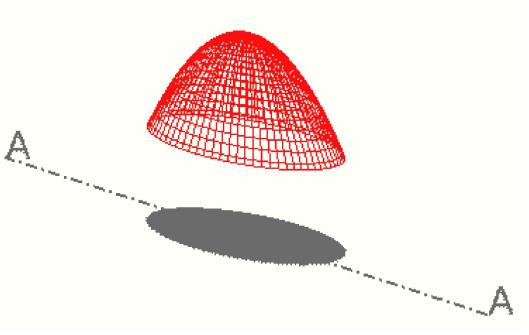

Figure 24: Parabolic load distribution along both directions of a wheel with elliptical tire-ground contact area (the A-A vertical section is taken along the cross-section of the wheel).

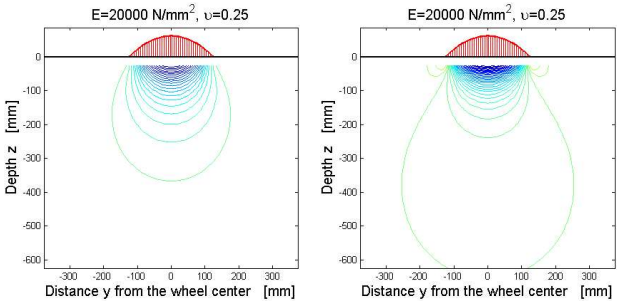

Figure 25: σ_z contours on the A-A vertical cross-section of Figure 24: Boussinesq's solution on the left and the second order solution on the right.

- The positive stresses arise near the contour of the contact area independently of the shape of the load profile.
- The maximum positive stresses arise at ends of the shorter diameter.
- The negative stresses of the second order solution are sensitively lower (in absolute value) than the negative stresses of Boussinesq's solution.
- The negative stresses concentrate along the directions of uniform load, under the ends of the load distribution, whereas they do not concentrate along the directions of parabolic load.

4 Numerical results of second order for two interacting distributed loads

In the lifetime of airfield pavements, lateral wander is an occurrence of particular importance. It arises because not all aircraft movements take place in the same position, for example, when taking off and landing. The position of

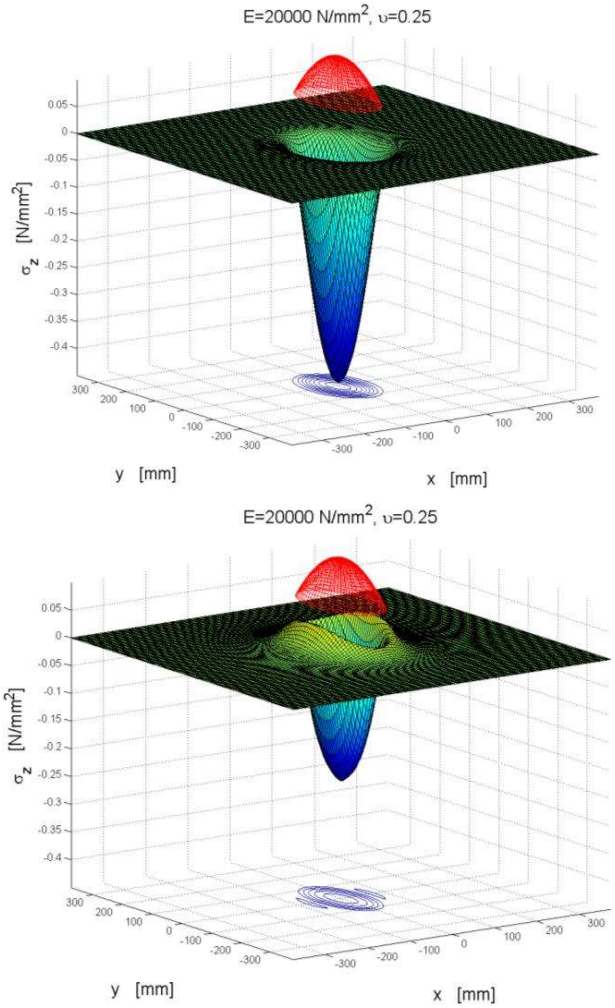

Figure 26: 3-D surfaces and stress contours of σ_z near the surface: Boussinesq's solution on the left and the second order solution on the right.

landing, for example, is influenced by the pilot's level of accuracy, cross-winds, width of runway, etc. Lateral wander has a significant influence on the rutting performance of airfield pavements, since individual aircraft wander patterns create traffic lanes. The wander width is defined by the zone containing 75% of the aircraft centerlines (1.15 standard deviations on either side of the mean value with a normal distribution). Taxiways are affected by a higher degree of traffic channelization than runways and traffic is also highly channelized at runway ends and on the turnoff areas between the runway to the taxiway or to the apron area.

Not only individual aircraft wander affects pavement performance. Aircrafts can have two or more landing gear systems offset at different positions from the body of the aircraft. Due to different gear assemblies (Figure 27), not

all aircrafts load the critical positions equally. Consequently, different aircraft combinations will induce additional wandering that is not associated to the lateral deviation of individual aircraft.

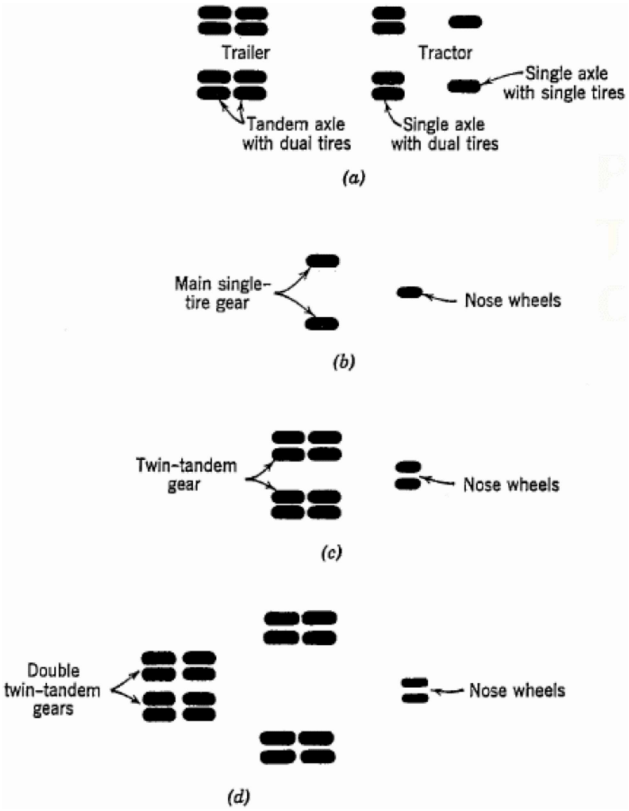

Figure 27: Plan view of: a) single trailer-truck unit; b) tricycle landing gear with single tires; c) twin-tandem landing gear; d) double twin-tandem landing gear (not to scale) (from [1]).

Moreover, in the light of the former discussion on the tensile stress field associated with the second order solution, we would expect that landing gear with twin wheels are especially detrimental to airfield pavements, since the short distance between the two wheels implies that the tensile stresses propagating on the surface, starting from the contour of the contact areas, will interact and increase in the portion of pavement enclosed between the wheels. This enhances the critical degree of the critical positions, especially when the wheels are set in a twin-tandem (Figures 27a and 27c) or double twin-tandem configuration (Figure 27d).

In the following part, we will examine the vertical stresses induced by twin wheels, such as those of the single axle in Figure 27a) and the nose wheels of Figures 27c) and 27d).

As we can see in Figure 29, for the simple interaction model of rectangular contact areas and uniform load (Figure 28), when obtaining the result for twin wheels numerically, the superficial stress profiles under the contact areas are equivalent to the juxtaposition of the stress profile on the right of Figure 14. Also in this case, we can appreciate the effect of negative stress concentrated at the ends of the two contact areas.

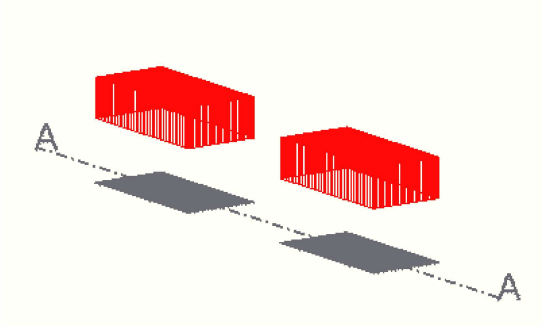

Figure 28: Uniform load distribution over the two rectangular tire-ground contact areas of a twin wheel (the A-A vertical section is taken along the cross-section of the twin wheel).

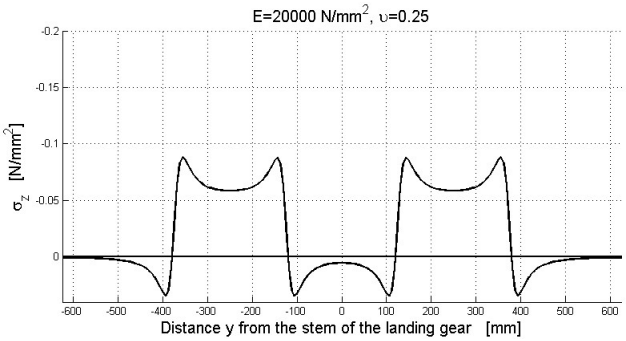

Figure 29: Superficial profiles of σ_z on the A-A vertical cross-section of Figure 28, according to the second order solution.

The positive stresses will also continue to concentrate near, but just outside, the ends of the contact areas, and rapidly decline on leaving the tires. Nevertheless, the inter-tire distance is too small for the positive stresses dampen completely between the two tires (Figure 29). Consequently, the pavement surface between the two tires is loaded in traction along all its extension. Due to the strong damping of the tensile stresses, however, the maximum tensile stress between the tires is almost the same as the maximum tensile stress outside the tires, indicating that the stress concentration at one end of the tire inter-space does not affect the stresses at the opposite end.

When compared with Figure 13, Figure 30, which contains the same number of contour lines as Figure 13, tells us that juxtaposing two tires on the pavement causes the contour lines to protrude more deeply into the pavement itself, both for the compressive stresses under the wheels and the tensile stresses between the wheels. This is due to the stress interaction caused by the juxtaposition. Note also that, outside the wheels, this interaction does not significantly modify the shape or the slope of the contour lines shown in green, which separate the family of the contour lines of traction from the family of the contour lines of compression. In conclusion, tire juxtaposition modifies the stress profiles at great depth, but not at the surface, except for that portion of surface enclosed between the tires.

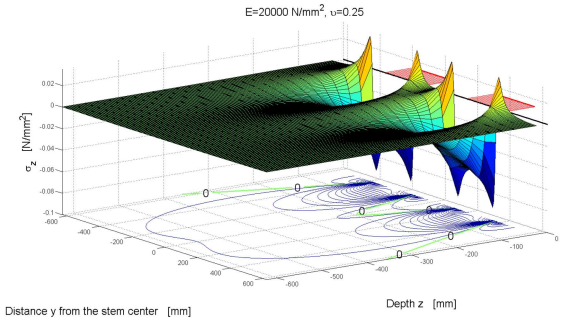

Figure 30: 3-D surface and stress contours of σ_z on the A-A vertical cross-section of Figure 28 (second order solution).

The superficial stress profiles are independent of tires juxtaposition also in Figure 31, where the 3-D stress profiles do not differ significantly from those of the single tire on the right of Figure 16, except for a slight difference in the portion of surface enclosed between the tires. The independence of the stress profile of one tire from the stress profile of another tire on the same surface is, consequently, not a property of a specific direction along the surface.

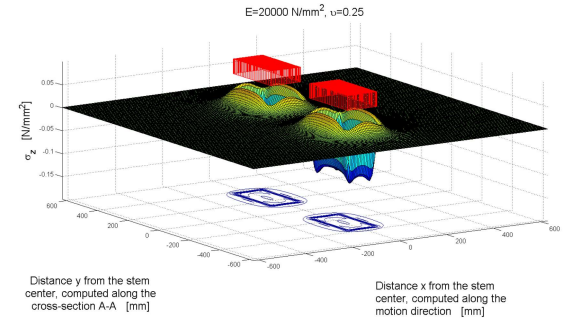

Figure 31: 3-D surfaces and stress contours of σ_z near the surface for the interaction model of Figure 28 (second order solution).

By changing the load profile from uniform to parabolic (Figure 32), the interaction between the two tires has the same particular features as in the former case (Figures 33 and 34):

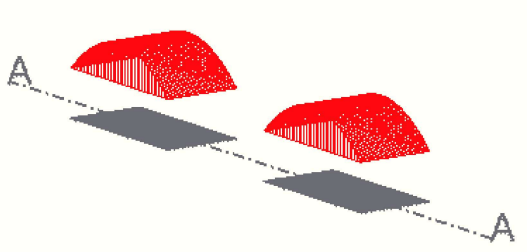

Figure 32: Parabolic load distribution along the cross-sections of a twin wheel with rectangular tire-ground contact areas (the A-A vertical section is taken along the cross-section of the twin wheel).

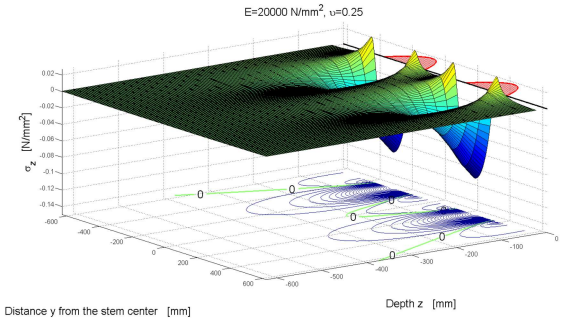

Figure 33: 3-D surface and stress contours of on the A-A vertical cross-section of Figure 32 (second order solution).

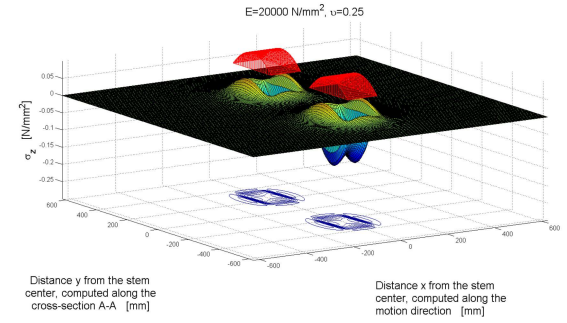

Figure 34: 3-D surfaces and stress contours of near the surface for the interaction model of Figure 32 (second order solution).

- the portion of surface enclosed between the two tires is entirely loaded in traction;

- the stress profiles are modified by tire juxtaposition at great depth, whereas they do not change at the surface, except for a slight difference in the portion of surface enclosed between the tires;
- the contour line $\sigma_z = 0$ is not modified by tire juxtaposition either in terms of shape or of slope.

One can draw the same conclusions when we change the contact area from rectangular to elliptical (Figures 35-40).

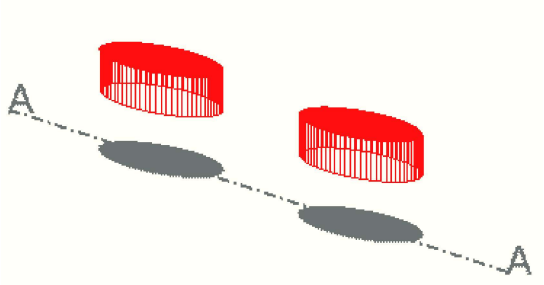

Figure 35: Uniform load distribution over the two elliptical tire-ground contact areas (the A-A vertical section is taken along the cross-section of the twin wheel).

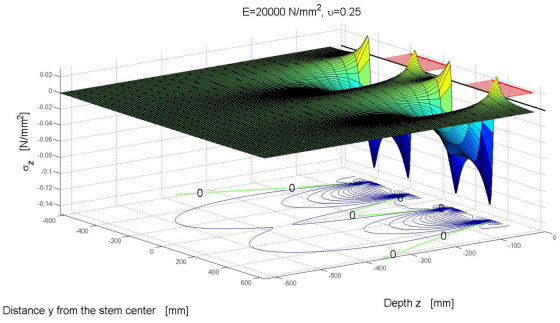

Figure 36: 3-D surface and stress contours of on the A-A vertical cross-section of Figure 35 (second order solution).

As a final remark, we must recall that no closed form solutions exist for a layered system, like an airfield pavement. The different approaches used to deal with layered elastic systems may be divided into:

- The Method of Equivalent Thicknesses (MET) [13], which transforms the layered system to semi-infinite half-spaces, on which Boussinesq's closed form solutions is usually used;
- Layered Analytical Models (LAM) [9], which are often referred to as mathematically exact solutions, where the fourth-order differential equation is

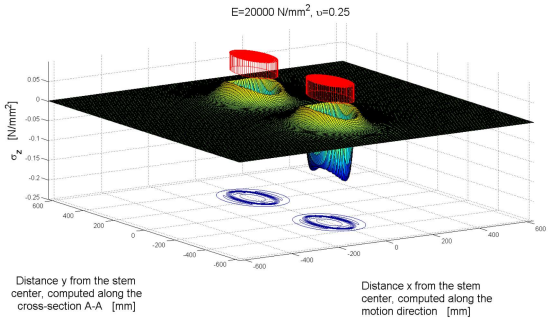

Figure 37: 3-D surfaces and stress contours of σ_z near the surface for the interaction model of Figure 35 (second order solution).

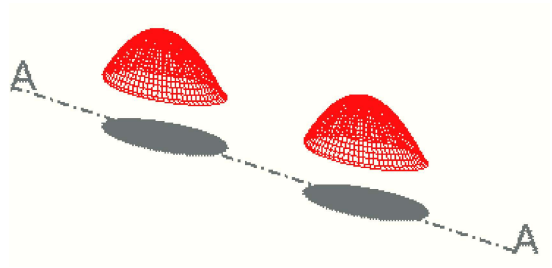

Figure 38: Paraboloid load distribution over the two elliptical tire-ground contact areas (the A-A vertical section is taken along the cross-section of the twin wheel).

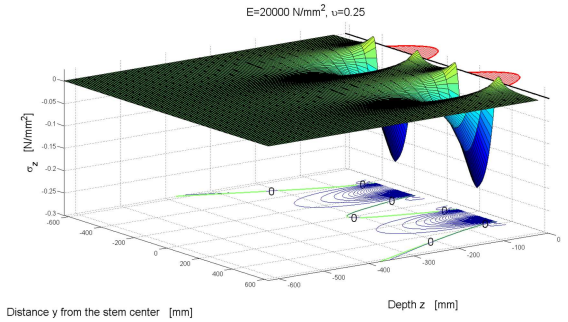

Figure 39: 3-D surface and stress contours of σ_z on the A-A vertical cross-section of Figure 38 (second order solution).

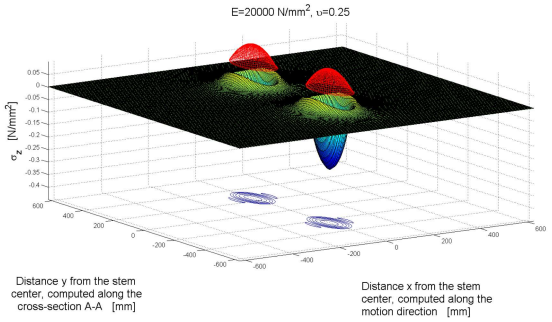

Figure 40: 3-D surfaces and stress contours of σ_z near the surface for the interaction model of Figure 38 (second order solution).

solved for the given boundary conditions using numerical integration;
- Finite Element Models (FEM), which divide a continuum into smaller more manageable elements, finite in size, each of which has its material behavior defined. The behavior of each element can be analyzed separately and the cumulative deformations of the elements brought together to give a resulting deformation for the whole structure.

Based on our results, Boussinesq's closed form solution is no more suitable to be used in MET for modeling layered elastic systems. It must be replaced with the second order closed form solution.

Moreover, stress and deflection values as obtained by Burmister in [9] are dependent upon the strength ratio of the layers. They are used to estimate development of pavement distress (rutting and fatigue cracking). Assuming the strength ratio equal to 1, it is possible to compare Burmister's analysis to that provided by a closed form solution. Well, although at great depths Burmister's and Boussinesq's analyses approach a common level, they are vastly different near the base-subgrade contact. Since Eqs. (27) and (28) show that even the exact solution gives the same result as Boussinesq at great depth while the two closed form solutions differ near the surface, we can regard the inconsistency between Burmister's and Boussinesq's analyses as an indirect proof that Boussinesq's solution does not comply with the boundary conditions for $z \to 0$. We can also expect that Burmister's results for the strength ratio equal to 1 are much more like the second order (exact) closed form solution than Boussinesq's closed form solution.

5 Conclusions

In this paper, we have argued that Boussinesq's closed form solution for a homogeneous, linear-elastic and isotropic half-space subjected to a point-load perpendicular to the surface is not the exact solution to Boussinesq's problem, since it does not satisfy the boundary conditions for stresses near the surface. In point of fact, at the time of Boussinesq the actual boundary condition for stresses at the surface was not known. Only recently technology has provided us with strain-gauges to be embedded into concrete for strain acquisition and stress identification [1], thus showing us that the solution of Boussinesq is not reliable near the surface. The recent experimental findings also allowed us to show that our new closed form elastic solution [6], built as an extension of the analytical strategy of Boussinesq to the second order solution, satisfies the boundary conditions along the entire contour of the half-space, thus representing the actual solution of Boussinesq's problem.

By way of example, we have provided and compared with experimental data some numerical results of the second order for rectangular and elliptical contact areas, loaded by uniform and parabolic laws of external pressure, for both single and twin wheels. The most interesting finding concerns the existence of a tensile state of stress near the contour of the contact areas, as in the case of point-load [6, 20], which makes the new rheological predictions adherent to the experimental acquisitions. In point of fact, also for contact areas greater than zero, the second order solution is composed of two families of stress contours on the vertical cross-section, one family for the tensile stresses and another for the compression stresses. This substantially modifies the first order solution of Boussinesq, which is composed of a single family of stress contours, the family of negative stresses.

We have also found that some characteristics of the stress profiles depend upon the model of the external load, whereas others do not. In particular, the superficial stress profiles of the negative stresses under the contact areas show two peaks near the contours of the contact areas exactly when the load profile on the vertical section is uniformly distributed. On the contrary, the tensile state of stress that arises near, but just outside, the contours of the contact areas does not depend on the shape of the load profile. In this latter case, in fact, the load profile simply enhances the positive peaks when it is uniformly distributed, but is not the main reason for the existence of these peaks. Indeed, their existence is a direct consequence of the second order solution of the problem of Boussinesq.

Moreover, juxtaposing two or more tires on the surface, like in the tandem configuration of a landing gear, does not seem to affect the superficial stress distribution significantly. It only modifies the stress profiles along the tire inter-surface – which turns out to be loaded in tension for all its extension – but does not enhance the positive peaks between the tires.

Things work differently in depth, since the juxtaposition of several tires seems to affect the stress profiles on a horizontal plane more significantly the greater the depth of the plane. However, this is not essential to the lifetime of airfield pavements, since they are designed to bear an increased state of negative stress.

What is actually detrimental to a pavement is the tensile state of stress near the surface [42]. At nowadays, in fact, airfield pavements are directly or indirectly designed

based on the solution of Boussinesq – which is inefficient in capturing the stress behavior near the surface, in general, and the tensile state of stress, in particular – and many of the pavement surface distresses are imputed to causes other than tensile stresses, notably, creep and viscosity. Consequently, there are no devices in place to prevent the pavement from tensile failure. The enhanced stress analysis provided by the exact closed form elastic solution will now allow us to state that those distresses may have origin just in the tensile state of stress near the contour of the contact areas and do not, as was believed until now, depend upon creep or viscosity (for a discussion on the relationship between crack and creep in concrete, see [43]).

6 Future developments

Our exact closed form elastic solution of Boussinesq's problem, together with new findings on the concrete constitutive behavior [43–52] may lead us to a better insight into performance of concrete airfield pavement and, ultimately, to more effective standards in their design. In point of fact, we must recall that the prediction of the propagation of the vertical stresses into the pavement and subsoil when carried by an aircraft, in particular, and a vertical load, in general, is an open question still now. In effect, according to the type of traffic loads and climatic conditions, the type of damage concerned, the structure considered, and the nature of the component materials, different types of response models are currently used for airfield pavements [1]. In order to avoid employing so many models, we can now study the layered system of any linear-elastic pavement by using MET [13] and our exact closed form solution of Boussinesq's problem for linear-elastic half-spaces. This should also close the gap between MET and LAM [9] solutions when the strength ratio of pavement layers is equal to 1.

Acknowledgement: The results presented here are part of the CIMEST Scientific Research on the Identification of Materials and Structures, DICAM, School of Engineering and Architecture, Alma Mater Studiorum, Bologna (Italy).

Funding: This research did not receive any specific grant from funding agencies in the public, commercial, or not-for-profit sectors.

References

[1] Ferretti, E., and M.C. Bignozzi, "Stress and Strain Profile along the Cross-Section of Waste Tire Rubberized Concrete Plates for Airport Pavements," CMC-Comput. Mater. Con. 27, 231-274 (2012).

[2] Ferretti, E., "Waste Tire Rubberized Concrete Plates for Airport Pavements: Stress and Strain Profiles in Time and Space Domains," CMC-Comput. Mater. Con. 31, 87-111 (2012).

[3] Giannakos, K., "Deflection of a railway reinforced concrete slab track: Comparing the theoretical results with experimental measurements," Eng. Struct. 122, 296-309 (2016).

[4] Boussinesq, M. J., Application des potentiels a l'étude de l'équilibre et du mouvement des solides élastiques, avec des notes étendues sur divers points de physique mathématique et d'analyse (Gauthier-Villars imprimeur libraire, Paris, 1885).

[5] Boussinesq, M. J., Essai théorique sur l'équilibre d'élasticité des massifs pulvérulents compare à celui de massifs solides et sur la poussée des terres sans cohesion (Mémoires des Savants Etrangers, Académie de Belgique, 40, Bruxelles, 1876).

[6] Ferretti, E., "A Higher Order Solution of the Elastic Problem for a Homogeneous, Linear-Elastic and Isotropic Half-Space Subjected to a Point-Load Perpendicular to the Surface," CMES-Comp. Model. Eng. 86, 435-468 (2012).

[7] Barker, W. R., and C. R. Gonzalez, Independent Evaluation of 6-Wheel Alpha Factor Report (Letter Report to the Federal Aviation Administration, U.S. Army Engineer Research and Development Center, Vicksburg, Mississippi, 2006).

[8] Binger, R. L., and L. G. Wells, Simulation of compaction from surface mining systems (ASAE Paper no. 89-2018, St. Joseph, MI: ASAE, 1989).

[9] Burmister, D. M., "The Theory of Stresses and Displacements in Layered Systems and Applications to the Design of Airport Runways," Proc. Highway Research Board 23, (1943).

[10] Caron, C., J. N. Theillout, and D. R. Brill, "Comparison of US and French Rational Procedures for the Design of Flexible Airfield Pavements," Proc. 2010 FAA Worldwide Airport Technology Transfer Conference, Atlantic City, New Jersey, USA, April 2010, 23 pp, (2010).

[11] Fröhlich, O. K., Druckverteilung im Baugrunde (Springer Verlag, Wien,1934).

[12] Gonzales, C. R., "Implementation of a New Flexible Pavement Design Procedure for U.S. Military Airports," Proc. Fourth LACCEI International Latin American and Caribbean Conference for Engineering and Technology (LACCEI'2006), Mayagüez, Puerto Rico, 21-23 June 2006, 10 pp, (2006).

[13] Odemark, N., Undersökning av elasticitetegenskaperna hos olika jordarter samt teori för beräkning av belägningar enligt elasticitetsteorin (Statens Väginstitut, meddelande 77, 1949).

[14] Seyrafian, S., B. Gatmiri, and A. Noorzad, "Analytical Investigation of Depth Non-homogeneity Effect on the Dynamic Stiffness of Shallow Foundations," CMES-Comp. Model. Eng. 21, 209-217 (2007).

[15] Sharifat, K., and R. L. Kushwaha, Modeling soil movement by tillage tools (Saskatoon, Saskatchewan Canada: Department of Agricultural and Bioresource Engineering, University of Saskatchewan, 2000).

[16] Söehne, W., "Fundamentals of pressure distribution and soil compaction under tractor tires," Agricultural Engineering 39,

276-281 (1958).
[17] Veverka, V., Modules, contraintes et déformations des massifs et couches granulaires (Rapport de Recherche, no. 162, vv, Centre de Recherches Routières, Bruxelles, 1973).
[18] Westergaard, H. M., "New Formulas for Stresses in Concrete Pavements of Airfields," ACE Transactions 108, also in (1947) ACE Proceedings 73, (1943).
[19] Hadamard, J., Sur les Problèmes aux Dérivées Partielles et leur Signification Physique (Princeton University Bulletin, 1902, 49-52).
[20] Ferretti, E., "The Second Order Solution of Boussinesq's Problem," Proc. SEMC 2013 – Research and Applications in Structural Engineering, Mechanics and Computation – Proc. 5th International Conference on Structural Engineering, Mechanics and Computation, 2473-2478, (2013).
[21] Ayers, P. D., and J. Van Riper, "Stress Distribution Under a Uniformly Loaded Rectangular Area in Agricultural Soils," Transactions of the ASAE – American Society of Agricultural Engineers 706-710 (1991).
[22] Fang, H. Y., J. Liu, and F. M. Wang, "A Precise Integration Method for Modeling GPR Wave Propagation in Layered Pavement Structure," CMES-Comp. Model. Eng. 99, 473-490 (2014).
[23] Olmstead T., and E. Fischer, Estimating Vertical Stress on Soil Subjected to Vehicular Loading (US Army Corps of Engineers, Engineer Research and Development Center, Cold Regions Research and Engineering Laboratory, ERDC/CRREL TR-09-02, Washington, 2009).
[24] Hartmann, S., R. Weyler, J. Oliver, J. C. Cante, and J. A. Hernández, "A 3D Frictionless Contact Domain Method for Large Deformation Problems," CMES-Comp. Model. Eng. 55, 211-270 (2010).
[25] Zhou, Y.-T., X. Li, D.-H. Yu, and K. Y. Lee, "Coupled Crack/Contact Analysis for Composite Material Containing Periodic Cracks under Periodic Rigid Punches Action," CMES-Comp. Model. Eng. 63, 163-190 (2010).
[26] Adler, A. A., and H. Reismann, "Moving Loads on an Elastic Plate Strip," J. Appl. Mech. 41,713–718 (1974).
[27] Law, S.-S., and X.-Q. Zhu, Moving Loads – Dynamic Analysis and Identification Techniques (Structures and Infrastructures Book Series 8, 2017).
[28] Dumitriu, D., L. Munteanu, C. Brisan, V. Chiroiu, R.-V. Vasiu, O. Melinte, and V. Vladareanu, "On the Continuum Modeling of the Tire/Road Dynamic Contact," CMES-Comp. Model. Eng. 94, 159-173 (2013).
[29] Jenq, S.-T., and Y.-S. Chiu, "Hydroplaning Analysis for Tire Rolling over Water Film with Various Thicknesses Using the LS-DYNA Fluid-Structure Interactive Scheme," CMC-Comput. Mater. Con. 11, 33-58 (2009).
[30] Carpinteri, A., M. Paggi, and G. Zavarise, "Cusp-Catastrophe Interpretation of the Stick-Slip Behaviour of Rough Surfaces," CMES-Comp. Model. Eng. 53, 303-326 (2009).
[31] Chen, Y. J., and N. Huber, "Transient Wear Simulation in Sliding Contacts of Spur Gear Teeth," CMC-Comput. Mater. Con. 29, 1-14 (2012).
[32] Chen, Y. J., and N. Huber, "Pressure-Force Transformation for Transient Wear Simulation in Two-Dimensional Sliding Contacts," CMC-Comput. Mater. Con. 16, 1-24 (2010).
[33] Misra, A., and S. Huang, "Micromechanics Based Stress-Displacement Relationships of Rough Contacts: Numerical Implementation under Combined Normal and Shear Loading," CMES-Comp. Model. Eng. 52, 197-216 (2009).
[34] Nairn, J. A., "Modeling Imperfect Interfaces in the Material Point Method using Multimaterial Methods," CMES-Comp. Model. Eng. 92, 271-299 (2013).
[35] Keerthika, B., Y. P. Cao, and D. Raabe, "Mechanical Characterization of Viscoelastic-Plastic Soft Matter Using Spherical Indentation," CMC-Comput. Mater. Con. 10, 243-258 (2009).
[36] Zhang, Q., and Q.-S. Yang, "The Analytical and Numerical Study on the Nanoindentation of Nonlinear Elastic Materials," CMC-Comput. Mater. Con. 37, 123-134 (2013).
[37] Füssl, J., W. Kluger-Eigl, and R. Blab, "Mechanical performance of pavement structures with paving slabs – Part I: Full-scale accelerated tests as validation for a numerical simulation tool," Eng. Struct. 98, 212-220 (2015).
[38] Füssl, J., W. Kluger-Eigl, and R. Blab, "Mechanical performance of pavement structures with paving slabs – Part II: Numerical simulation tool validated by means of full-scale accelerated tests," Eng. Struct. 98, 221-229 (2015).
[39] Spangler, M. G., Stresses in Concrete Pavement Slabs (Transportation Research Board of the National Academies – Highway Research Board Proceedings 14, 1935).
[40] Hossain, M., A. Muqtadir, and A. M. Hoque, "Three-Dimensional Finite Element Analysis of Concrete Pavement System," Journal of Civil Engineering, the Institution of Engineers, Bangladesh CE 25 33-47 (1997).
[41] Darestani, M. Y., D. P. Thambiratnam, D. Baweja, and A. Nataatmadja, "Dynamic Response of Concrete Pavements under Vehicular Loads," Proc. IABSE Symposium, Budapest, Hungary, 8 pp. (2006).
[42] Ferretti, E., "A Cell Method stress analysis in thin floor tiles subjected to temperature variation," CMC-Comput. Mater. Con. 36, 293-322 (2013).
[43] Ferretti, E., and A. Di Leo, "Cracking and Creep Role in Displacement at Constant Load: Concrete Solids in Compression," CMC-Comput. Mater. Con. 7, 59-80 (2008).
[44] Ferretti, E., "Shape-Effect in the Effective Laws of Plain and Rubberized Concrete," CMC-Comput. Mater. Con. 30, 237-284 (2012).
[45] Ferretti, E., "Cell Method Analysis of Crack Propagation in Tensioned Concrete Plates," CMES-Comp. Model. Eng. 54, 253-281 (2009).
[46] Ferretti, E., "On Nonlocality and Locality: Differential and Discrete Formulations," Proc. ICF XI, 11th International Conference on Fracture, Turin (Italy), March 20-25, 6 pp. (2005).
[47] Ferretti, E., "A Local Strictly Nondecreasing Material Law for Modeling Softening and Size-Effect: a Discrete Approach," CMES-Comp. Model. Eng. 9, 19-48 (2005).
[48] Ferretti, E., "A Discussion of Strain-Softening in Concrete," Int. J. Fracture 126, L3-L10 (2004).
[49] Ferretti, E., "Experimental Procedure for Verifying Strain-Softening in Concrete," Int. J. Fracture 126, L27-L34 (2004).
[50] Ferretti, E., "On Poisson's Ratio and Volumetric Strain in Concrete," Int. J. Fracture 126, L49-L55 (2004).
[51] Ferretti, E., "On Strain-Softening in Dynamics," Int. J. Fracture 126, L75-L82 (2004).
[52] Ferretti, E., "A Discrete Nonlocal Formulation Using Local Constitutive Laws," Int. J. Fracture 130, L175-L182 (2004).
[53] Ferretti, E., A. Di Leo, and E. Viola, "Computational aspects and numerical simulations in the elastic constants identification," Problems in Structural Identification and Diagnostics: General Aspects and Applications, Book Series: CISM Courses and Lec-

tures 471, 133-147 (2003).
[54] Ferretti, E., A. Di Leo, and E. Viola, "A novel approach for the identification of material elastic constants," Problems in Structural Identification and Diagnostics: General Aspects and Applications, Book Series: CISM Courses and Lectures 471, 117-131 (2003).